Gardner, L. and Nethercot, D. A. (2004). Numerical modeling of stainless steel structural components – A consistent approach. Journal of Structural Engineering-ASCE. **130(10)**, 1586-1601.

NUMERICAL MODELING OF STAINLESS STEEL STRUCTURAL COMPONENTS – A CONSISTENT APPROACH

By L. Gardner[1] and D. A. Nethercot[2]

KEY WORDS (from ASCE thesaurus)

finite elements, flexural strength, hollow sections, imperfections, numerical models, residual stress, stainless steel

ABSTRACT

This paper describes numerical modeling of the structural response of stainless steel hollow sections. The aim of the investigation was to develop a consistent approach to the modeling of stainless steel structures. The developed FE models are more sophisticated than any other reported attempts to model stainless steel structural behavior, with general expressions defined for material stress-strain behavior, enhanced strength corner properties, initial geometric imperfection modes and amplitudes (local and global), and residual stresses. The general expressions define a consistent means of describing the key input parameters. A compound (two-stage) Ramberg-Osgood model is developed to describe stainless steel material stress-strain behavior in tension and compression. For the prediction of enhanced strength corner properties, a simple, though accurate model is proposed. Characterization of local plate imperfection amplitudes is described whereby a model originally devised for hot-rolled carbon steel cross-sections was re-calibrated and applied to stainless steel cross-sections. Numerical prediction of the key performance measures from tests is achieved with a high degree of accuracy: On average, ultimate load was predicted to within 3% and with a low standard deviation; deformation at ultimate load was within 6%, but exhibited a higher standard deviation; and the general form of the load-deformation response and the failure modes were similar.

INTRODUCTION

Due to the expense and impracticalities of generating comprehensive structural performance data through experimentation, structural engineers are turning increasingly to numerical modeling. Previous attempts to model

[1] Lecturer, Department of Civil and Environmental Engineering, Imperial College London, South Kensington Campus, London SW7 2AZ, UK. Email: leroy.gardner@imperial.ac.uk
[2] Head of Department, Professor, Department of Civil and Environmental Engineering, Imperial College London, South Kensington Campus, London SW7 2AZ, UK. Email: d.nethercot@imperial.ac.uk

stainless steel structures have tended to be overly simplistic, and only validated against a relatively small sample of test results. Furthermore, there has been little consistency between the approaches adopted in different studies.

This paper presents a consistent approach to the numerical modeling of stainless steel hollow section members subjected to compression, bending and combined compression plus bending. General expressions and methods to define the key input parameters for the modeling of the material stress-strain behavior, cold-worked corner properties, residual stresses and initial geometric imperfections are described. Validation of the models is made against all existing test data, and parametric studies to investigate the influence of key variables are presented. Results from the numerical study were used in the development and verification of a new design method for stainless steel structural components, described by Gardner et al. (2003). The general-purpose finite element (FE) software package ABAQUS (2002) was employed throughout the study.

MATERIAL MODELING

Description of stress-strain behavior

Material modeling generally represents one of the most important aspects of an FE simulation. Inaccurate or inappropriate modeling of the basic material behavior of a structure will overshadow the performance of even the most refined FE models.

Stainless steel exhibits a rounded stress-strain curve, with no sharp yield point, that is most commonly described by an expression originally proposed by Ramberg and Osgood (1943), and modified by Hill (1944).

$$\varepsilon = \frac{\sigma}{E_0} + 0.002\left(\frac{\sigma}{\sigma_{0.2}}\right)^n \tag{1}$$

where σ and ε are engineering stress and strain, respectively, E_0 is the material Young's modulus, $\sigma_{0.2}$ is the material 0.2% proof stress and n is a strain hardening exponent. A review of other material models and investigation into their applicability to stainless steels was made by Gardner (2002).

Limitations in the basic Ramberg-Osgood expression at higher strains and when applying it to compressive stress-strain data have been observed by a number of authors (Mirambell and Real, 2000, Gardner and Nethercot, 2001 and Rasmussen, 2003). A modification to the basic Ramberg-Osgood expression was proposed by Mirambell and Real (2000) whereby the single curve defined by Equation 1 was replaced by a two-stage model, incorporating two

Ramberg-Osgood curves. In their proposed model, Mirambell and Real (2000) adopted the basic Ramberg-Osgood expression up to the 0.2% proof stress. Beyond the 0.2% proof stress and up to ultimate stress, a second Ramberg-Osgood curve was used. The origin of the second curve was defined at the 0.2% proof stress, and continuity of magnitude and gradient was ensured at the transition point. Further work on this two-stage model was conducted by Rasmussen (2003) where the additional parameters required by the two-stage model were described in terms of the original Ramberg-Osgood parameters ($\sigma_{0.2}$, E_0 and n) following analysis of stainless steel stress-strain data.

Gardner and Nethercot (to be published1) recognized the value of the Mirambell and Real proposal, but noted that use of the ultimate stress, σ_u in the second phase of the model (between $\sigma_{0.2}$ and σ_u) has two drawbacks. Firstly, since the strain at σ_u is far higher than those strains concurrent with general structural response, greater deviation between measured and modeled material behavior results than if a lower strain was used. Secondly, and more importantly, the model is not applicable to compressive stress-strain behavior, since there is no ultimate stress in compression, due to the absence of the necking phenomenon.

Gardner and Nethercot (to be published1) therefore proposed that the 1% proof stress be used in place of the ultimate stress, leading to Equation 2. Equation 1 continues to apply for stresses up to $\sigma_{0.2}$.

$$\varepsilon = \frac{(\sigma - \sigma_{0.2})}{E_{0.2}} + \left(0.008 - \frac{\sigma_{1.0} - \sigma_{0.2}}{E_{0.2}}\right)\left(\frac{\sigma - \sigma_{0.2}}{\sigma_{1.0} - \sigma_{0.2}}\right)^{n'_{0.2,1.0}} + \varepsilon_{t0.2} \qquad (\sigma \geq \sigma_{0.2}) \qquad (2)$$

where $n'_{0.2,\,1.0}$ is a strain hardening coefficient representing a curve that passes through $\sigma_{0.2}$ and $\sigma_{1.0}$.

Equation 2 provides excellent agreement with experimental stress-strain data, both in compression and tension, up to strains of approximately 10%, and was therefore adopted for the material model used in all numerical analyses.

Corner material properties

General

The stress-strain properties of the corner regions in cold-formed stainless steel cross-sections differ from the properties of the flat regions due to the material's response to deformation. Stainless steel exhibits pronounced

strain hardening, resulting in corner regions of cold-formed square and rectangular hollow sections (SHS and RHS, respectively) having 0.2% proof strengths commonly between 20% and 100% higher than the 0.2% proof strengths of the flat regions, accompanied by a corresponding loss in ductility.

Gardner and Nethercot (to be published1) have reviewed previous work in this area and observed that because the corner material has been work-hardened to a sufficient extent to be operating in the relatively flat part of the material stress-strain curve (typically strains between 10 and 20%), the 0.2% proof strength of the corner material, $\sigma_{0.2,c}$ may be expressed as a fixed percentage of the ultimate stress of the flat material, σ_u. Based on the available test data (Gardner, 2002 and Rasmussen and Hancock, 1993) this was found to be around 85% and thus the simple proposal of Equation 3 was made.

$$\sigma_{0.2,c} = 0.85\sigma_u \tag{3}$$

Despite its simplicity, Equation 3 was found to fit the available test data rather well and is therefore used for generating the corner material properties in the FE models described throughout this paper.

RESIDUAL STRESSES

Introduction

Residual stresses are introduced into cold-formed stainless steel members as a result of the deformations during the cold-forming fabrication process, and due to the thermal gradients that are induced during (seam) welding.

Measurements of residual stresses in cold-formed stainless steel cross-sections are scarce. Knowledge of the magnitude and distribution of residual stresses within a cold-formed stainless steel cross-section is therefore speculative. Some measurements were taken by Rasmussen and Hancock (1993) as part of an experimental programme on cold-formed stainless steel tubular members.

Due to the inherent uncertainty associated with residual stress magnitudes and distributions, their effect is often taken into account in numerical models with an appropriate increase in the magnitude of initial geometric imperfection. In this study, an approximate, though representative solution to the modeling of residual stresses in cold-formed stainless steel CHS, SHS and RHS is sought.

Deformationally induced residual stresses

Deformationally induced residual stresses in carbon steel cross-sections have been investigated experimentally and analytically by Ingvarsson (1975, 1979), Weng and Peköz (1988), Abdel-Rahman and Sivakumaran (1997) and Schafer and Peköz (1998). Rasmussen and Hancock (1993a) investigated deformationally induced residual stresses in stainless steel hollow sections, and observed that the tension and compression coupons cut from finished tubes curved longitudinally as a result of the through-thickness bending residual stresses. This same phenomenon was observed in the current study (Gardner, 2002). The effect of these residual stresses is to cause premature yielding through part of the material thickness, thus altering the response of structural components. However, elastic straightening of the coupons as part of the testing procedure approximately re-introduces the bending residual stresses. Therefore, provided that material properties are established from coupons cut from within the cross-section, the effects of bending residual stresses will be inherently present, and do not have to be explicitly defined in the FE model.

Thermally induced residual stresses

Thermally induced residual stresses resulting from welding have been thoroughly investigated in the past. A detailed account of their formation and effects on carbon steel cross-sections has been given by Lay and Ward (1969). Stainless steel has a higher coefficient of thermal expansion, and a lower value of thermal conductivity than carbon steel. It is therefore expected that thermal residual stresses would be greater in stainless steel cross-sections. Bredenkamp et al. (1992) found that the magnitudes of residual stresses in built up stainless steel I-sections were of the same order as in an equivalent carbon steel section, whilst Lagerqvist and Olsson (2001) carried out a similar study and observed considerably higher residual stresses in the stainless steel sections.

For the modeling of welding residual stresses in cold-formed SHS and RHS stainless steel cross-sections, it is proposed to apply the simplified distribution shown in Figure 1 to the welded face of the cross-section.

The half width, c of the tension area for a single continuous weld was given by Young (1974), following tests on Grade 43 carbon steel as Equation 4.

$$c = 50\,\alpha\,\frac{A}{\Sigma t}\,\frac{235}{\sigma_y} \tag{4}$$

where A is the cross-sectional area of added metal, Σt is the sum of the plate thicknesses meeting at the weld, and α is the process efficiency factor, suggested as 0.90 for submerged arc welding, 0.80 for manual welding and 0.62 for MIG (spray) welding. In the absence of the weld details, a width of b/5 (where b is the plate width) can be assigned to the tensile residual stress area (Masubuchi, 1980).

Assuming the magnitude of the tensile residual stress area is taken as yield (or the 0.2% proof stress), self-equilibrium of axial forces requires Equation 5 to hold, where σ_{rt} and σ_{rc} are the tensile and compressive residual stresses respectively.

$$\sigma_{rc} = \sigma_{rt} \frac{2c}{b-2c} \tag{5}$$

Measurements of weld-induced residual stresses in carbon steel CHS have been made by Chen and Ross (1977) and Ostapenko (1977). Typical results from the Chen and Ross study are shown in Figure 2, where the dashed line represents their proposed linear residual stress pattern. No measurements of weld-induced residual stresses are available for stainless steel CHS.

Based on the measurements taken by Chen and Ross, Gao et al. (1998) proposed a simpler stress-block model, which was successfully applied to the FE modeling of short steel cylinders in compression and bending. Their proposed projected residual stress distribution is shown in Figure 3. This distribution was adopted for the modeling of weld-induced residual stresses in cold-formed stainless steel CHS (with $\sigma_{0.2}$ used in place of σ_y).

INITIAL IMPERFECTIONS

For close replication of observed structural behavior, knowledge of both the distribution and magnitude of cross-sectional and member imperfections is required. This is a complex function of the rolling and fabrication process, with sufficient variability between cross-sections to have precluded their definitive characterization. Very close agreement between the behavior of FE models and experiments can be achieved by the superposition of imperfection modes, with the magnitudes determined by means of parametric studies. Sully and Hancock (1999) described how sympathetic and unsympathetic local imperfections were combined with an overall imperfection, to calibrate an FE model to experiments on cold-formed tubular cross-sections.

However, for the generation of further results from parametric studies, and to investigate trends in areas that are not supported by experimental results, a general imperfection that is representative of cold-formed stainless steel hollow sections is sought. Its suitability can be established through comparison with available experimental data.

Local imperfection mode

SHS and RHS

For convenience in both hand and numerical analyses, the shape of a local initial geometric imperfection is often assumed to be the same as that of the lowest buckling mode, or eigenmode (Dawson and Walker, 1972). This shape of imperfection is also the most severe in terms of local buckling behavior since it coincides with the deflected shape that would occur in a buckled perfect plate. The lowest buckling mode, generated from an elastic eigenmode analysis of each of the cold-formed stub columns, was therefore used as the initial imperfection mode. It should be noted that no clear local imperfection mode emerged from the experimental data. The four lowest buckling modes from an eigenmode analysis of an SHS 80×80×3 are shown in Figure 4 (a) to (d).

CHS

As for the SHS and RHS, the local imperfection shape for the CHS stub columns was taken as the lowest buckling mode from an eigenmode analysis. For all modeled cases the lowest eigenmode comprised a sinusoidal curve in both the longitudinal and circumferential directions. Wheeler and Bridge (2000) conducted a detailed analysis of the effect of imperfection modes and magnitudes on the behavior of thin-walled steel CHS filled with concrete. Their total imperfection included local and global components generated from eigenmode buckling analyses.

Global imperfection mode

For the FE modeling of pin-ended columns that fail by overall flexural buckling, a global imperfection that corresponded to the lowest buckling mode (generated from an elastic eigenmode analysis) was adopted. For a column where the ends are free to rotate this is a single half-sine wave. The complete initial imperfection field therefore comprised a superposition of the local and global modes.

SHS and RHS local imperfection amplitude

The amplitude of local plate imperfection has an important influence on the behavior of stub columns, though measurements of initial imperfections are commonly omitted from experimental programmes. An investigation into the prediction of measured imperfection amplitudes was carried out.

Observations

Local imperfection amplitudes on the faces of SHS and RHS stub column specimens were measured for 15 different cross-section sizes. Towards the ends of the stub columns the faces of the cross-sections were distorted by bending residual stresses. The magnitudes of initial imperfection in these end regions are consequently relatively high, though they are not representative of the overall out-of-flatness of the faces of the stub columns. By adopting imperfections of the magnitude observed at the stub column ends it was found that the FE models consistently under-predicted the strength and deformation capacity of the corresponding test. It was therefore decided to investigate the initial imperfections that were present over the less distorted central three-quarter portion of the stub columns. The datum for the initial imperfection measurements is taken as the line connecting the 3/4 points of the stub column.

For each cross-section size, imperfection measurements were generally conducted on two independent specimens. Although imperfection data exhibits notoriously high scatter, Figure 5 shows that there is a good degree of consistency between the independent measurements. The tendency for specimen 2 imperfections to be higher than specimen 1 imperfections has no significance.

Prediction of imperfection amplitude

The simplest means of predicting the amplitude of an initial plate imperfection, ω_0 is as a fixed multiple of the plate thickness, i.e. $\omega_0 = Kt$, where K is a constant. Dawson and Walker (1972) showed that an adequately conservative fit to test data on cold-formed steel cross-sections could be achieved with an imperfection amplitude of 0.2t, though they recognized that an imperfection amplitude defined as a fixed multiple of the plate thickness is unsuitable as a general parameter for all plates. A further expression given in Equation 6 was also shown to be unsuitable as a general parameter. It was concluded that an imperfection amplitude of the form given in Equation 7 was more rational than the previous two expressions, and was in agreement with current rolling practice. It should be noted that the 0.2% proof stress, $\sigma_{0.2}$ has been used in place of the yield stress, σ_y in Equations 6 and 7 to enable application to stainless steel. Dawson and Walker found that a value of $\gamma = 0.2$ gave reasonable fit to test data for simply-supported plates, and square hollow sections. Square hollow sections produce no constraining moments

between the elements of the cross-section due to their symmetrical nature. Their behavior therefore closely corresponds to an assemblage of simply-supported plates (Timoshenko and Gere, 1985).

$$\omega_0 / t = \alpha(\sigma_{0.2}/ \sigma_{cr})^{0.5} \quad (6)$$

$$\omega_0 / t = \gamma(\sigma_{0.2}/ \sigma_{cr}) \quad (7)$$

where ω_0 is the initial imperfection amplitude, t is the plate thickness, $\sigma_{0.2}$ is the material 0.2% proof stress, σ_{cr} is the plate critical buckling stress and α and γ are constants. Chou et al. (2000) conducted FE modeling of cold-formed lipped channel and hat-section carbon steel stub columns with varying imperfection amplitudes. The study showed that Equation 7 yielded the most accurate and consistent prediction of experimental behavior as compared to three other imperfection amplitudes of 0.1, 0.5 and 1.0 times the material thickness.

Schafer and Peköz (1998) presented some rules of thumb for the prediction of the maximum local imperfection in a stiffened element that apply for a width-to-thickness ratio less than 200, and a material thickness of less than 3mm. A simple linear regression analysis based on plate width, w yielded Equation 8, and an alternative rule based on an exponential fit to the thickness was given as Equation 9, where ω_0 is the amplitude of the initial imperfection, w is the width of the plate, and t is the thickness of the plate in mm.

$$\omega_0 \approx 0.006w \quad (8)$$

$$\omega_0 \approx 6te^{-2t} \quad (9)$$

Based on observations, Schafer and Peköz (1998) also applied a probabilistic approach to the characterization of imperfection amplitudes. For a stiffened element, a mean imperfection of 0.50 times the material thickness was generated, with a standard deviation of 0.66. This is, however, too simple an analysis to have general applicability. The suitability of applying Equations 6 and 7 to the prediction of imperfection amplitudes in cold-formed stainless steel members (measured in the current study) was assessed. The values of α and γ were adjusted to fit the experimental results.

As Dawson and Walker noted for cold-formed carbon steel members, Equation 6 was also found to be unsuitable for the prediction of imperfection amplitudes in cold-formed stainless steel members. A linear regression analysis revealed that best fit is achieved with $\alpha = 7.3 \times 10^{-6}$ with a corresponding coefficient of determination R^2 equal to

0.025. The R^2 parameter is a sound indicator of whether a postulated relationship gives a good approximation to observed data. The closer the R^2 value is to unity the better the prediction. A similar linear regression analysis was conducted based on Equation 7, revealing that best fit is achieved with $\gamma = 0.023$ (leading to Equation 10), with a corresponding R^2 value of 0.22. A comparison between the measured and predicted (Equation 10) imperfection amplitudes is presented in Figure 6.

$$\omega_0 / t = 0.023(\sigma_{0.2}/ \sigma_{cr}) \quad (10)$$

Since the two wider faces of RHS possess a higher level of edge restraint (provided by the two shorter, stiffer sides of the cross-sections) it would be expected that the amplitude of imperfections would be lower than for a corresponding face of an SHS. The data points, however, demonstrated little justification for including edge restraint in the predictive model. Equation 10 is therefore employed for the generation of local imperfection amplitudes in numerical models of all SHS and RHS members.

Tables 1 and 2 compare predicted values of maximum imperfection amplitude with measured values for SHS and RHS specimens respectively. The mean of the tensile and compressive values for E_0 and $\sigma_{0.2}$ have been used in the predictive model for each cross-section.

Although the predictions in Tables 1 and 2 exhibit a relatively high degree of scatter, it is demonstrated in Table 3 that the FE models using these predicted imperfections still produce accurate agreement with test results, though, in general, careful consideration should be given to any FE model's sensitivity to imperfections.

CHS local imperfection amplitude

The available imperfection data for stainless steel CHS were too limited to enable the development of a relationship between initial imperfection amplitude and the geometric and material properties of a cross-section. The importance of local imperfection amplitude was therefore assessed by means of a parametric study, and a suitable imperfection amplitude to use for the generation of further results was found. Local imperfection amplitudes of 0.01t, 0.1t, 0.2t and 0.5t (where t is the material thickness) were assessed. The parametric study revealed that the most accurate replication of the key performance indicators from test results of ultimate load and deformation at ultimate load was achieved with a local imperfection amplitude of 0.2t. This is clearly, however, a simple model with limited scope; further experimental and numerical work is required to develop a model for local imperfections in CHS of the sophistication of Equation 10 (for flat elements)

Global imperfection amplitude

The effect of global imperfection amplitude on the flexural buckling of columns was also assessed by means of a parametric study. To establish a representative global imperfection amplitude, a parametric study was conducted. A set of 12 pin-ended columns, tested as part of the current investigation and covering a range of cross-sectional slendernesses, $\beta = (b/t)\sqrt{\sigma_{0.2}/E_0}$, (where b and t are plate width and thickness, respectively and $\sigma_{0.2}$ and E_0 are material 0.2% proof stress and Young's modulus, respectively) and non-dimensional global slendernesses, $\overline{\lambda}$, were modeled using three imperfection amplitudes: L/1000, L/2000 and L/5000. Comparisons of ultimate load carrying capacity from the tests and FE models were made. It was found that a global imperfection amplitude of L/2000 resulted in the most accurate agreement between FE ultimate load and test ultimate load, with an average value of FE ultimate load divided by test ultimate load of 1.00 with a standard deviation of 0.07. It should also be noted that the sensitivity to changes in imperfection magnitude between the range of L/1000 to L/5000 was low, with average values of FE ultimate load divided by test ultimate load of 0.96 and 1.03 for L/1000 and L/5000, respectively.

A further study was conducted to investigate the imperfection sensitivity of a 2m SHS 80×80×4 pin-ended column for a range of global imperfection amplitudes from L/100 to L/10000. With a non-dimensional slenderness, $\overline{\lambda}$ close to unity, the 2m SHS 80×80×4 pin-ended column falls into the band of traditionally associated with high sensitivity to imperfections. The results are shown in Figure 7.

From Figure 7 it can be seen that for global imperfection amplitudes of less than L/1000, the variation in ultimate load carrying capacity is relatively small (≈10%). However, for higher imperfection amplitudes the ultimate load carrying capacity begins to drop off much more sharply. It is recommended that, where available, measured global imperfections amplitudes be used, though in the absence of such measurements an amplitude of L/2000 may be applied based on the results of the current study.

SHS AND RHS STUB COLUMN MODELING

Introduction

As part of the parallel experimental programme, a total of 33 SHS and RHS stub columns were tested to provide data on cross-section deformation capacity over a broad range of cross-sectional slenderness. The purpose of the FE modeling of SHS and RHS stub columns was to replicate test behavior, to investigate the influence of key parameters, to establish definitive values/ models for key parameters and to act as a basis for the modeling of member behavior.

Development of SHS and RHS FE models

The general-purpose FE package ABAQUS (2002) was employed for all the numerical modeling conducted in this study. Models used measured geometry, measured and predicted initial plate imperfections, assumed residual stresses and measured and predicted material properties, with enhanced material properties employed in the corner regions.

The elements chosen for the stub column models were 9-noded, reduced integration shell elements with five degrees of freedom per node, designated as S9R5 in the ABAQUS element library. This element has been shown to perform well in similar applications involving the modeling of stainless steel SHS and RHS flexural members (Real, 2001) and the buckling response of mild steel and high performance steel box columns in axial compression (Kiymaz, 1999). S9R5 is characterized as a 'thin' shell element and is not recommended for modeling cases where transverse shear flexibility is important. Transverse shear flexibility is said to become important when the shell thickness is more than about 1/15 of a characteristic length on its surface (ABAQUS, 2002). All except the stockiest stub column cross-sections that are modeled in this study have width-to-thickness ratios greater than 15. For consistency, the S9R5 shell element has been adopted for all modeled cases, though it is recognized that for the stockiest cross-sections the large strain formulation of the S4R 'thick' shell element may give more reliable results.

The curved geometry at the corners of the cross-sections has been modeled using curved S9R5 shell elements. Convergence studies were conducted to decide upon a suitable mesh density, with the aim of achieving suitably accurate results whilst minimizing computational time. From this study, it was found that approximately 8 elements across the plate widths and a maximum element aspect ratio of two yielded high accuracy.

Linear elastic eigenmode simulations were conducted to provide buckling modes to be used as initial imperfections in subsequent non-linear analyses, as described in Section 4.4. The modified Riks method (ABAQUS, 2002) was employed to solve the geometrically and materially non-linear stub column models. The modified Riks method is an algorithm that enables effective solutions to be found to unstable problems (e.g. post-ultimate response of stub columns), and adequately traces non-linear unloading paths.

For each stub column, the full length and half of the cross-section was modeled, with symmetry boundary conditions prescribed along the vertical edges. The ends of the stub columns were fixed against all degrees of freedom except for vertical displacement at the loaded end. All boundary conditions are depicted in Figure 8. Equations were used to constrain the nodes at the loaded end of the stub columns to move vertically in unison. Nodal loads were applied to the constrained node set.

ABAQUS requires that material behavior is specified by means of a multi-linear stress-strain curve, defined in terms of true stress and log plastic strain, using the *PLASTIC command. The relationships between true stress and engineering stress, σ_{true} and σ_{nom}, respectively, and log plastic strain and engineering strain, ε_{ln}^{pl} and ε_{nom}, respectively, are given in Equations 11 and 12 respectively. Engineering stress and strain are the nominal values that are recorded from a uniaxial stress-strain coupon test.

$$\sigma_{true} = \sigma_{nom} (1 + \varepsilon_{nom}) \quad (11)$$

$$\varepsilon_{ln}^{pl} = \ln (1 + \varepsilon_{nom}) - \frac{\sigma_{true}}{E} \quad (12)$$

Average measured compressive properties are used for the flat regions of the cross-sections, and average measured tensile corner properties for the corner regions (since no tests were conducted on corner coupons in compression).

For some of the stub column tests conducted as part of other laboratory testing programmes values for $\sigma_{1.0}$ and $n'_{0.2,1.0}$ in compression were not available. In these cases the value of $\sigma_{1.0}$ is taken as a multiple of $\sigma_{0.2}$, found from the mean of all other available test data to be $\sigma_{1.0} = 1.26\sigma_{0.2}$, and similarly $n'_{0.2,1.0}$ is taken as 2.7, which is the absolute mean value from all other available test data.

Where no measurements of corner properties were taken, predicted values (from Equation 3) were adopted. In the absence of strain hardening parameters for corner material n_c (equivalent to n for flat material) and $n'_{0.2,1.0,c}$ (equivalent to $n'_{0.2,1.0}$ for flat material), absolute mean values from all other available test data were used. This provided $n_c = 4.3$ and $n'_{0.2,1.0,c} = 4.6$.

Extent of corner regions

The degree to which the enhanced corner properties extend beyond the curved corner portions of the cross-sections is unclear. Karren (1967) found that for carbon steel sections the effect of cold-forming extends beyond the corner to a distance approximately equal to the material thickness, t. However, stainless steels exhibit far more pronounced strain hardening than carbon steels so it may be assumed that extension to a distance t is a lower bound. Abdel-Rahman and Sivakumaran (1997) observed increased yield strengths at a distance of $0.5\pi r_i$ from the curved corner

portions of cold-formed carbon steel cross-sections, though of lower magnitude than in the curved portions themselves.

A parametric study was conducted to investigate the behavior of cold-formed stainless steel stub columns with enhanced strength regions extending to t and 2t beyond the curved corner portions, as shown in Figure 9. For the annealed specimens uniform flat material properties were assumed around the whole cross-section. The results are given in Table 3. For each comparison the measured stub column geometry, measured initial imperfections and assumed residual stresses remained constant.

Table 3 presents a summary of a comparison between FE results and test results for all SHS and RHS stub columns. A total of 48 stub column tests were modeled with the results obtained from Rasmussen and Hancock (1993), Talja and Salmi (1995) and Gardner and Nethercot (to be published1). Overall, modeling accuracy is very good.

The influence of the corner properties can also be clearly seen in Table 3. It can be concluded that FE models (using measured initial geometric imperfection amplitudes) with corner properties extended to 2t beyond the curved portions of the cross-sections yield better agreement with test results than FE models with corner properties extended only to a distance t. FE models with no allowance for corner strength enhancements produce average under-predictions of strength of around 8%.

In the absence of measured initial imperfection data, predicted values must be utilized. From Table 3 it may be seen that results generated using predicted initial imperfection amplitudes (from Equation 10) do not differ significantly from those generated using measured amplitudes. With predicted imperfections the mean ultimate strength shows an increase of approximately 1.5%, and the mean deformation at ultimate strength shows an increase of approximately 7%. The stub column ultimate strength exhibits less variability than the deformation at ultimate strength (reflected by the lower standard deviation). This is therefore perhaps a better measure of the integrity of the models. It should be noted that deformations at ultimate strength are sensitive to parametric variations (in the tests and FE models) since the slope of the load-deformation curves are low in this region, with small increments of load corresponding to large increments in deformation.

Influence of residual stresses

Residual stresses of magnitude and distribution as described above were implemented into the stub column models using the ABAQUS ∗INITIAL CONDITIONS command. Prior to the application of external loading, a preliminary

load step to allow equilibration of the residual stresses was defined. No residual stresses were included in the models of the annealed specimens because it was assumed that any residual stresses due to welding would have been relieved during the annealing process. However, it is recognized that thermal residual stresses due to non-uniform cooling of the cross-sections may have been introduced.

A study into the sensitivity of the stub column models to residual stresses was conducted. Simulations were run with and without residual stresses whilst other parameters remained constant. Figures 10 and 11 show typical load versus end shortening curves.

The effect of the residual stresses is clear, causing a small reduction in stiffness of the stub columns but having little influence on their overall behavior or ultimate load carrying capacities.

Failure modes

All tested stub columns failed with the same characteristic failure mode whereby the four faces of the cross-sections buckled locally alternately outwards and inwards. Similar failure modes were observed in the FE models. Figure 12 shows a typical failed stub column with its corresponding FE model.

Discussion

In general, good agreement between test and FE model behavior has been displayed. Figures 13 and 14 show the variation in FE and test results for a range of cross-section slendernesses, $\beta = (b/t)\sqrt{\sigma_{0.2}/E_0}$. It can be seen that the greatest discrepancies between observed and modeled behavior occur at the extremities of the tested range of slenderness, and that the prediction of deformations shows the greater variation. At low slenderness, the discrepancies are believed to be due to inaccuracies generated by the large plastic strains. This may be overcome, as described earlier, by employing 'thick' shell elements. At high slenderness, it is believed that the imperfection sensitivity associated with the post-buckling response of slender compression elements produces the large scatter of results.

With successful replication of cross-sectional behavior, modeling of more complex overall member behavior, which involves an interaction between local (cross-sectional) effects and global (member) effects can now be conducted.

CHS STUB COLUMN MODELING

Background

Results from tests on CHS stub columns loaded in pure compression are relatively scarce. The purpose of the FE modeling of CHS stub columns was therefore to replicate the available test results and to generate further load-deformation data by means of parametric studies.

Development of FE models

Development of the CHS stub column FE models was similar to that for the SHS and RHS stub columns, with a few exceptions. Element choice, material modeling, boundary conditions, generation of initial geometric imperfection modes, and analysis types were as for the SHS and RHS models. A typical CHS stub column FE model is shown in Figure 15.

Material properties were assumed to be uniform around the cross-section, since test results for material extracted from different parts of the cross-sections exhibited little variation, and with no discernible pattern. The weld-induced residual stress distribution described earlier was adopted, and the effect of these residual stresses is demonstrated.

Influence of residual stresses

Residual stresses of magnitude and distribution as earlier were implemented into the CHS stub column models in the same manner as for the SHS and RHS stub columns. Simulations were run with and without residual stresses to assess the sensitivity of the models to their presence. Typical results are shown in Figure 16 for a CHS 100×1.0.

As expected, the effect of the residual stresses on the CHS stub column models is similar to the SHS and RHS case, causing a small reduction in initial stiffness but having little influence on overall behavior or ultimate load carrying capacities.

Influence of initial geometric imperfection amplitude

Cylinders with relatively low diameter-to-thickness (D/t) ratios are generally referred to as tubes or pipes, whereas those with relatively high D/t ratios are referred to as shells. Shells subjected to axial compression buckle chiefly in the elastic material range and are often extremely sensitive to the presence of imperfections. CHS used for structural applications (and examined in the current study) have relatively low D/t ratios and failure is largely

controlled by (gradual) material yielding. For such cases, sensitivity to changes in geometric imperfections is significantly lessened.

A parametric study was conducted to determine a suitable geometric imperfection amplitude for stainless steel CHS. FE simulations of all stainless steel CHS stub column tests were conducted with four different levels of imperfection amplitude, specified as a proportion of the material thickness, t. The four imperfection amplitudes, ω_0 were 0.01t, 0.1t, 0.2t and 0.5t. Results are shown in Table 4. The study revealed that that CHS stub column behavior was most accurately replicated with an initial geometric imperfection amplitude of 0.2t. Stub column deformation capacity at ultimate load, which is the key parameter of interest, was shown to be well predicted with a standard deviation comparable to that which exists between repeated laboratory test results.

Generation of further results

With satisfaction in the ability of the FE models to replicate test results, a parametric study was conducted to generate results over a range of cross-sectional slendernesses to support the test data. A CHS with an outer diameter of 100 mm, a length of 350 mm, material stress-strain properties as for the CHS 101.6×2.85 (tested by Rasmussen and Hancock), and an initial geometric imperfection amplitude of 0.2t was chosen as the basis for the parametric study. These parameters were fixed, and variation in cross-section slenderness was achieved through variation in material thickness. The results of the study were used by Gardner and Nethercot (to be published1) in conjunction with all available test results to develop a relationship between cross-section slenderness and cross-section deformation capacity, to act as a basis for a new structural design method for stainless steel.

SHS AND RHS PIN-ENDED COLUMN MODELING

Background

It has been shown that the behavior of stainless steel SHS and RHS stub columns can be accurately replicated using the described modeling techniques and assumptions. This demonstrates the ability to predict the load-carrying and deformation response to variation in cross-sectional slenderness. The behavior of pin-ended columns is more complex and is dependant upon overall member slenderness, cross-sectional slenderness and the interaction between local and global phenomena.

Development of FE models

Development of the FE models for pin-ended columns was similar to that for stub columns. Models included measured geometry, measured and predicted initial plate imperfections and initial overall members imperfections,

assumed residual stresses and measured and predicted material properties, with enhanced material properties applied to the corner regions. The same 9-noded, reduced integration shell elements, S9R5 were adopted for the modeling of the stainless steel members.

The cross-sectional parameters were selected based on the findings from the stub column FE modeling study. Curved S9R5 shell elements were used to model the curved corner regions of the cross-sections, and enhanced corner material properties were assumed to extend to a distance of 2t (two times the material thickness) beyond the curved regions. The incorporation of residual stresses and initial plate imperfections followed the stub column assumptions. Where measurements of local plate imperfection amplitude were not available, predicted amplitudes (given by Equation 10) were used. Global imperfection amplitudes of L/2000 were adopted in all flexural buckling models.

Linear elastic eigenmode simulations were conducted to generate both the local and global imperfection modes, and a superposition of the two gave the final imperfection pattern. The lowest local and global buckling modes generally appeared in the first few eigenmodes. Figure 17 shows the two lowest eigenmodes for a 1m pin-ended RHS 100×50×3. Non-linear analyses employed the modified Riks method.

Column end plates were modeled using the ABAQUS multi-purpose C3D20 20-node quadratic brick elements. Nodes along one centreline of the outer surfaces of both end plates were fixed against all degrees of freedom, except for minor axis rotation at both ends and vertical displacement at the loaded end. This provided pin-ended conditions in the minor axis buckling direction. Similar boundary conditions were used across the perpendicular centerlines to model major axis buckling. Constraint equations were employed to ensure that there were no end rotations about the non-buckling axis, and loads were introduced through the constrained node sets.

Effect of residual stresses

Residual stresses were included in the pin-ended column FE models in the same manner as for the stub columns. A parametric study to investigate the sensitivity of the pin-ended column models to residual stresses was conducted. Simulations were run with and without residual stresses whilst other parameters remained constant. Figure 18 shows the resulting load versus lateral deflection curves for a 2m pin-ended SHS 100×100×4 column.

The influence of residual stresses on pin-ended column SHS flexural buckling behavior can be seen from Figure 18 to be relatively insignificant. A small reduction in stiffness can be observed prior to ultimate load, but the ultimate load carrying capacity itself is unaffected.

Comparison between test and FE results

A comparison of ultimate load carrying capacity for all tests and FE models of pin-ended SHS columns is presented in Table 5. Similarly, comparisons for all pin-ended RHS columns buckling about the minor and the major axis are presented in Tables 6 and 7 respectively. A total of 28 pin-ended SHS and RHS column tests were modeled, with the test results obtained from Rasmussen and Hancock (1993), Talja and Salmi (1995) and Gardner and Nethercot (to be published2).

Discussion

Overall the agreement between test and FE results for flexural column buckling is satisfactory. An obvious exception to this is the SHS 80×80×3-LC3 (tested by Rasmussen and Hancock) with an FE F_u/Test F_u ratio of 1.49, and to a lesser extent the SHS 80×80×3-LC2 (tested by Rasmussen and Hancock) with a FE F_u/Test F_u ratio of 1.25. In both cases, the test failure loads are significantly below those predicted by the FE models.

Gardner (2002) made a comparison between the test failure loads and those predicted by Eurocode 3 and the proposed design method. Both design methods predict failure loads in close agreement with the FE results, and therefore showing similarly large deviation from the test results. No problems with the testing procedure or the test results were reported by Rasmussen and Hancock.

SHS AND RHS BEAM MODELING

Introduction

Sufficient test results for stainless steel beams failing by in-plane bending are available to preclude the need for extensive FE modeling in this area. However, no test results are available on RHS beams either where the proportions of the cross-section are such that local buckling occurs in the web, or where the beam is subject to lateral torsional buckling. The proportions of structural hollow sections are such that both of these cases are unusual. Nonetheless, for completeness, a study was conducted to investigate the applicability of Eurocode buckling coefficients to the inelastic local buckling of the webs of stainless steel beams of extreme proportions. However, it was decided not to model stainless steel RHS beams with proportions and loading conditions conducive to lateral torsional buckling, since the structural behavior is complex and there are no supporting test data to use for validation. Results from the study (Gardner, 2002) indicated that the Eurocode coefficients were broadly applicable, though with increasing usage of RHS with high aspect ratio, further experimental and numerical verification is required.

SHS AND RHS PIN-ENDED BEAM-COLUMN MODELING

Introduction

Beam-columns are members subjected to a combination of applied axial loads plus applied bending moments (about either or both of the principal axes). The design of such members involves consideration of the individual loading components

No tests on beam-columns were conducted as part of the current study, but a total of 12 tests were reported by Talja and Salmi (1995). FE modeling of these tests was conducted using the parameters found from the stub column and pin-ended column modeling.

Development of FE models

The SHS and RHS beam-column FE models were similar to the pin-ended column models, with the exception of the point of load introduction. For the beam-columns, the load was applied eccentrically, through the centreline of the wall thickness of the cross-section. Figure 19 shows the restraints adopted to create pin-ended boundary conditions.

Comparison with test results

A comparison of ultimate load carrying capacity for all tests and FE models of pin-ended SHS and RHS beam-columns is presented in Table 8. It should be noted that for all tested RHS beam-columns, bending was about the major axis.

Discussion

The results exhibit excellent agreement between test and FE behavior. This confirms that the parameters derived from the stub column and pin-ended column models are equally applicable to the modeling of stainless steel SHS and RHS beam-columns.

CONCLUSIONS

This paper has described the FE modeling of stainless steel CHS, SHS and RHS members subjected to a variety of loading arrangements. Key parameters and methods have been defined through examination of experimental data and through carefully conducted parametric studies to achieve a consistent approach to the modeling. A summary of the findings is listed below:

- Material stress-strain properties were described by means of a compound (two-stage) Ramberg-Osgood formulation (defined by Equations 1 and 2)

- Enhanced corner material properties in SHS and RHS were defined (Equation 3), and found (by means of parametric studies) to extend to a distance of 2t beyond the curved portions of the cross-sections

- A suitable amplitude of local initial geometric imperfections was found to be defined by Equation 10 for SHS and RHS (determined from analysis of imperfection data, and by comparison of stub column test and FE results), and taken as 0.2t for CHS (following parametric studies with varying imperfection amplitude and comparison with stub column test results)

- Initial member out-of-straightness was taken as L/2000 following parametric studies and comparison with test results

- Representative residual stress distributions were defined for CHS, SHS and RHS sections, but parametric studies showed their influence to be relatively insignificant within the context of column response

- For all problem types (stub columns, pin-ended columns and beam-columns), for which reliable test data exists, the numerical predictions of the key performance measures demonstrated a high degree of accuracy: On average, ultimate load was predicted to within 3% and with a low standard deviation; deformation at ultimate load was within 6%, but exhibited a higher standard deviation; and the general form of the load-deformation response and the failure modes were similar.

Overall, it can be concluded that the ABAQUS-based FE models developed in this study represent a sound and cost-effective alternative to physical testing as a means of predicting the full load-deformation response of stainless steel structural members whose behavior may involve a combination of local and overall buckling.

ACKNOWLEDGEMENTS

The authors are very grateful to EPSRC and the AvestaPolarit UK Research Foundation for the project funding, and would like to thank Nancy Baddoo and Bassam Burgan from The Steel Construction Institute and David Dulieu from the AvestaPolarit UK Research Foundation for their technical support. Thanks should also be extended to Kim Rasmussen from the University of Sydney, Asko Talja from VTT Building Technology Finland, and Esther Real from the Universitat Politècnica de Catalunya, for their help in providing their test programme details.

REFERENCES

ABAQUS (2002). ABAQUS/ Standard User's Manual Volumes I-III and ABAQUS CAE Manual. Version 6.3. Hibbitt, Karlsson and Sorensen, Inc. Pawtucket, USA.

Abdel-Rahman, N. and Sivakumaran, K. S. (1997). Material properties models for analysis of cold-formed steel members. Journal of Structural Engineering, ASCE. **123:9**, 1135-1143.

Bredenkamp, P. J., Van den Berg, G. J., and Van der Merwe, P. (1992). Residual stresses and the strength of stainless steel I-section columns. Proceedings of the Structural Stability Research Council, Annual Technical Session. Pittsburg, U.S.A. 69-86.

Chen, W. F. and Ross, D. A. (1977). Test of fabricated tubular columns. Journal of Structural Division, ASCE. **103:3**, 619-634.

Chou, S.M., Chai, G. B. and Ling, L. (2000). Finite element technique for design of stub columns. Thin-Walled Structures. **37**, 97-112.

Dawson, R. G. and Walker, A. C. (1972). Post-buckling of geometrically imperfect plates. Journal of the Structural Division, ASCE. **98: ST1**, 75-94.

Gao, S., Usami, T. and Ge, H. (1998). Ductility of steel short cylinders in compression and bending. Journal of Engineering Mechanics, ASCE. 124:2, 176-183.

Gardner, L. (2002). A new approach to stainless steel structural design. PhD Thesis. Structures Section, Department of Civil Engineering, Imperial College, London.

Gardner, L. and Nethercot, D. A. (2001). Numerical modelling of cold-formed stainless steel sections. Proceedings of the Ninth Nordic Steel Construction Conference. Edited by Mäkeläinen et al. Helsinki, Finland. 781-789.

Gardner, L. Nethercot, D. A. and Estrada, I. (2003). An efficient method for designing stainless steel structures. Proceedings of the Structural Stability Research Council Annual Technical Session and Meeting. Baltimore, USA. 473-492.

Gardner, L. and Nethercot, D. A. (to be published1). Experiments on stainless steel hollow sections – Part 1: Material and cross-sectional behaviour. Journal of Constructional Steel Research.

Gardner, L. and Nethercot, D. A. (to be published2). Experiments on stainless steel hollow members – Part 2: Behaviour of columns and beams. Journal of Constructional Steel Research.

Hill, H. N. (1944). Determination of stress-strain relations from the offset yield strength values. Technical Note No. 927, National Advisory Committee for Aeronautics. Washington, D.C.

Ingvarsson, L. (1975). Cold-forming residual stresses. Effect on buckling. Proceedings of the Third Speciality Conference on Cold-formed Steel Structures. 85-119.

Ingvarsson, L. (1979). Cold-forming residual stresses in thin-walled structures. Proceedings of the First International Conference on Thin-Walled Structures. University of Strathclyde, Glasgow. 575-587.

Karren, K. W. (1967). Corner properties of cold-formed steel shapes. Journal of the Structural Division, ASCE. **93:ST1**, 401-432.

Kiymaz, G. (1999). Stability criteria for thin-walled box columns of high performance steel in axial compression. PhD Thesis. Structures Section, Department of Civil Engineering, Imperial College, London.

Lagerqvist, O. and Olsson, A. (2001). Residual stresses in welded I-girders made of stainless steel and structural steel. Proceedings of the Ninth Nordic Steel Construction Conference. Edited by Mäkeläinen et al. Helsinki, Finland. 737-744.

Lay, M. G., and Ward, R. (1969). Residual stresses in steel sections. Journal of the Australian Institute of Steel Construction. **3:3**, 2-21.

Masubuchi, K. (1980). Analysis of welded structures. Pergamon Press Ltd.

Mirambell, E. and Real, E. (2000). On the calculation of deflections in structural stainless steel beams: an experimental and numerical investigation. Journal of Constructional Steel Research, **54**, 109-133.

Ostapenko, A. (1977). Local buckling of welded tubular columns. Report No. 406.11. Fritz Engineering Laboratory, Lehigh University, Bethlehem, Palestine.

Ramberg, W. & Osgood, W. R. (1943). Description of stress-strain curves by three parameters. Technical Note No. 902, National Advisory Committee for Aeronautics. Washington, D.C.

Rasmussen, K. J. R. (2003). Full range stress-strain curves for stainless steel alloys. Journal of Constructional Steel Research. 59, 47-61.

Rasmussen, K. J. R. and Hancock, G. J. (1993). Design of cold-formed stainless steel tubular members. I: Columns. Journal of Structural Engineering, ASCE. **119: 8**, 2349-2367.

Real, E. (2001). Aportaciones al estudio del comportamiento a flexion de estructuras de acero inoxiddable. Tesis Doctoral. Departamento de Ingeniería de la Construcción, Universitat Politècnica de Catalunya. UPC-ETSECCP. Barcelona, Mayo. (In Spanish).

Shafer, B. & Peköz, T. (1998). Computational modelling of cold-formed steel: characterizing geometric imperfections and residual imperfections. Journal of Constructional Steel Research. **47**, 193-210.

Sully, R. M. & Hancock, G. J. (1999). Stability of cold-formed tubular beam-columns. Proceedings of the Fourth International Conference on Steel and Aluminium Structures, ICSAS '99. Edited by Mäkeläinen, P. and Hassinen, P. Espoo, Finland. 141-154.

Talja, A. and Salmi, P. (1995). Design of stainless steel RHS beams, columns and beam-columns. Research Note 1619, VTT Building Technology, Finland.

Weng, C. C. & Pekoz, T. (1988). Residual stresses in cold-formed steel members. Proceedings of the Ninth International Speciality Conference on Cold-Formed Steel Structures. St. Louis, Missouri, U.S.A. 167-189.

Wheeler, A. T. & Bridge, R. Q. (2000). Thin-walled steel tubes filled with high strength concrete in bending. Proceedings of the Composite Construction IV Conference. Alberta, Canada.

Young, B. W. (1974). The effect of process efficiency on the calculation of weld shrinkage forces. Proceedings of the Institution of Civil Engineers, Part 2. **57**, 685-692.

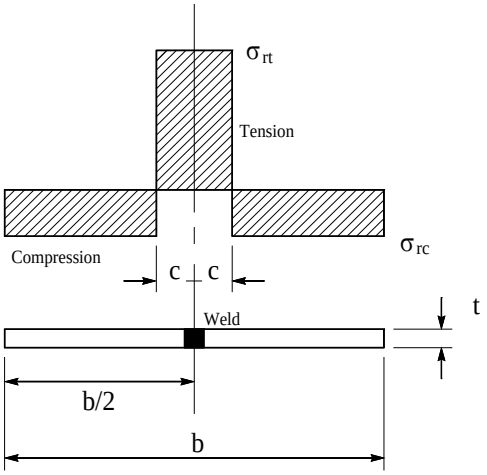

Figure 1: Idealized weld-induced residual stress distribution for SHS and RHS

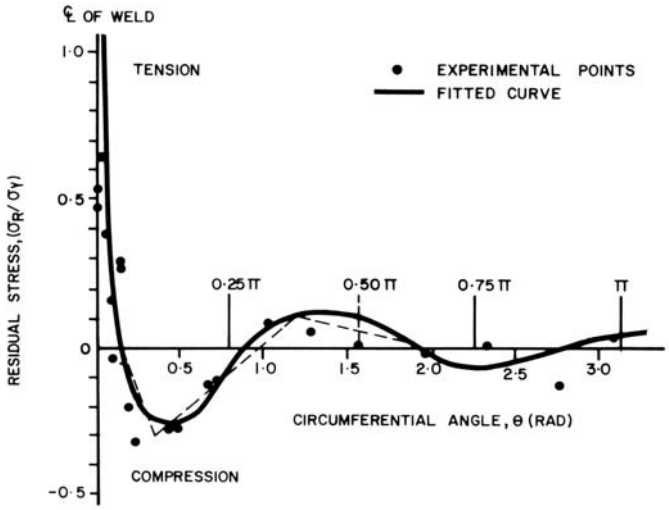

Figure 2: Residual stress measurements in welded carbon steel CHS (Chen and Ross, 1977)

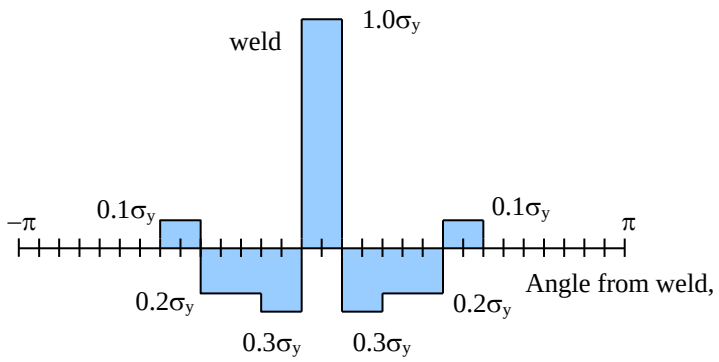

Figure 3: Projected CHS residual stress model proposed by Gao et al. (1998)

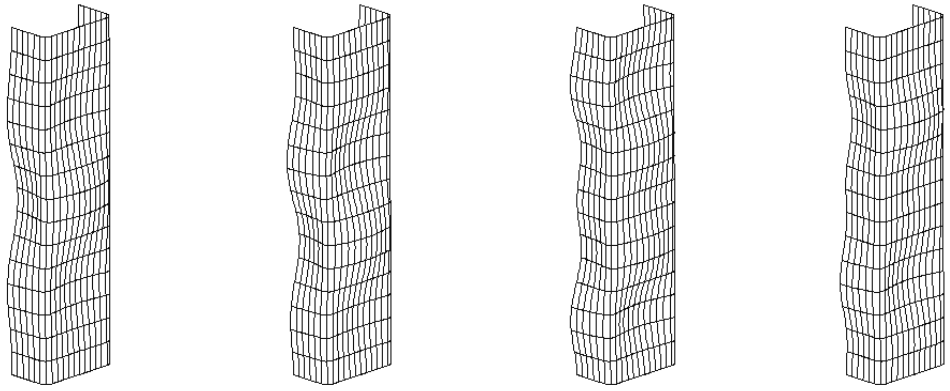

(a) Eigenmode 1 (b) Eigenmode 2 (c) Eigenmode 3 (d) Eigenmode 4

Figure 4: Four lowest eigenmodes for an SHS 80×80×3 stub column

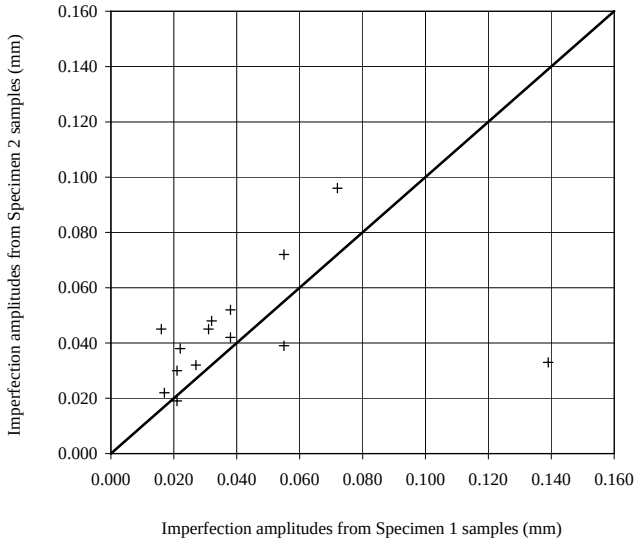

Figure 5: Comparison of imperfection amplitudes from independent specimens

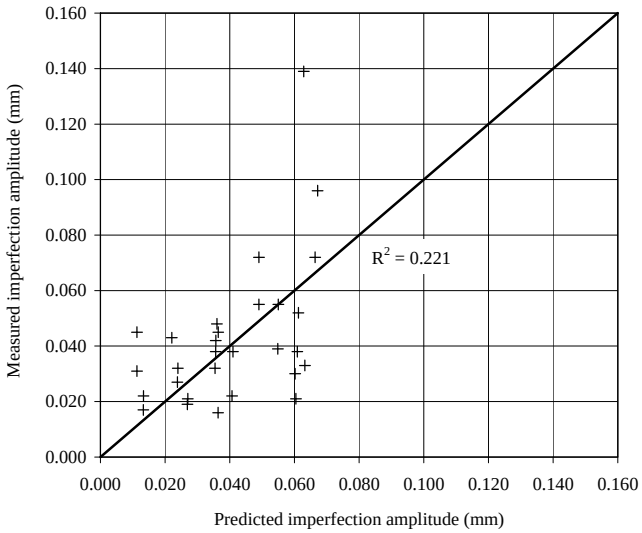

Figure 6: Measured versus predicted imperfection amplitudes for $\omega_0 / t = 0.023(\sigma_{0.2} / \sigma_{cr})$

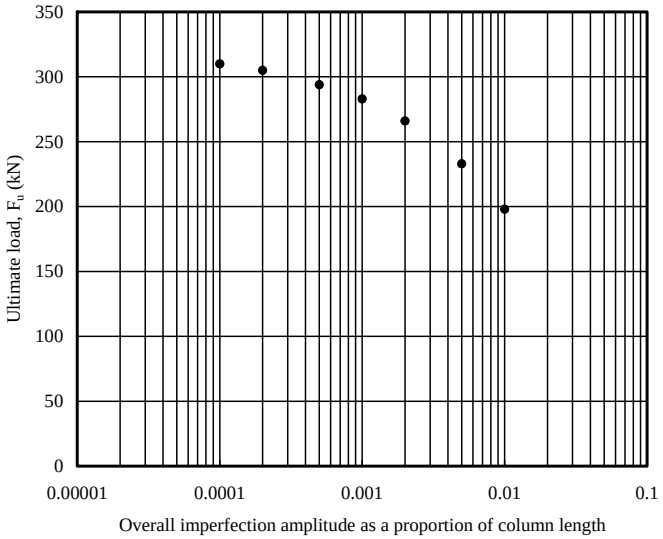

Figure 7: Imperfection sensitivity of 2m SHS 80×80×4 pin-ended column for global imperfection amplitudes ranging from L /100 to L /10000

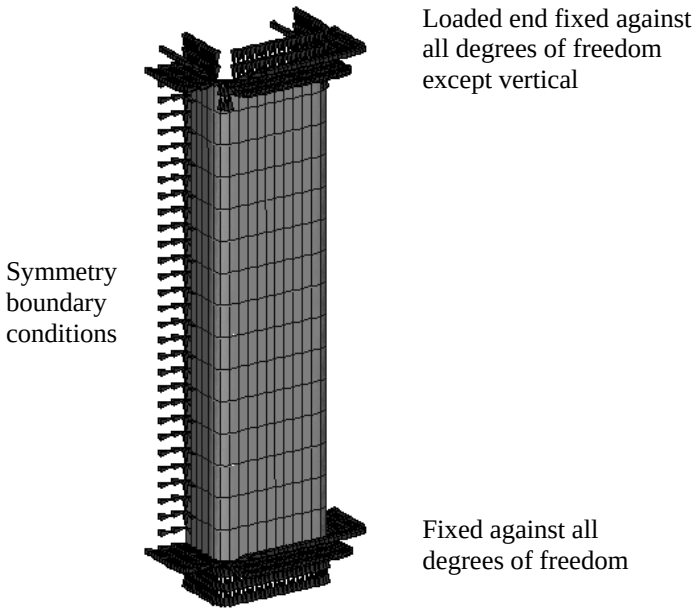

Figure 8: Boundary conditions applied to SHS and RHS stub column FE models

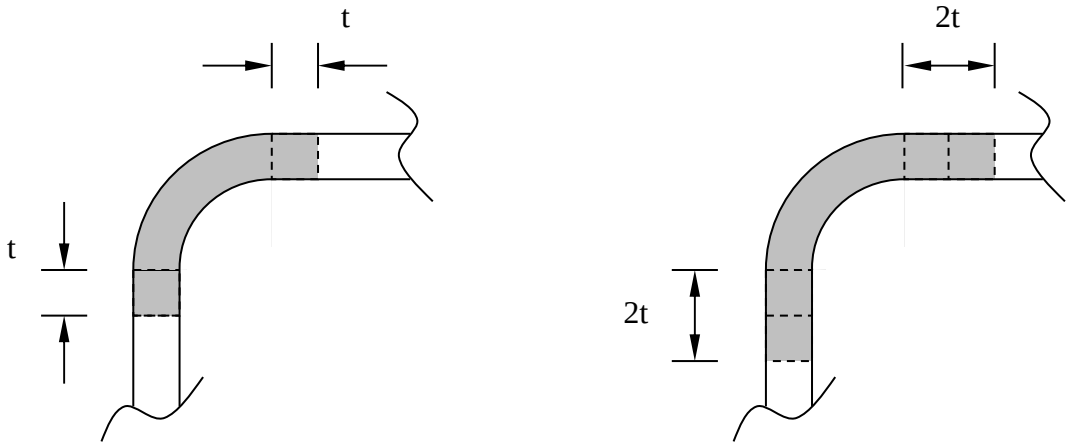

(a) Corner properties extended to a distance t beyond curved portion

(b) Corner properties extended to a distance 2t beyond curved portion

Figure 9: Extents of corner regions in FE models

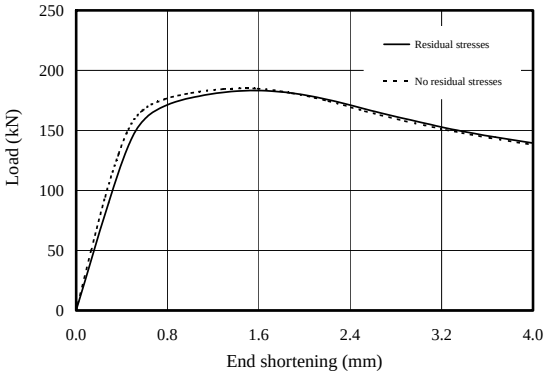

Figure 10: Effect of residual stresses on 100×100×2 stub column FE model

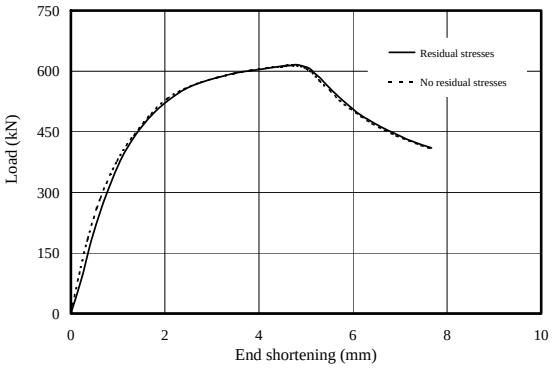

Figure 11: Effect of residual stresses on 80×80×4 stub column FE model

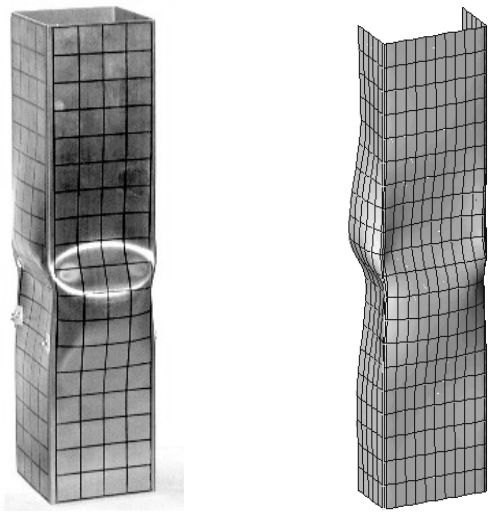

Figure 12: Failure mode from SHS 100×100×2- SC1 stub column test and corresponding FE model

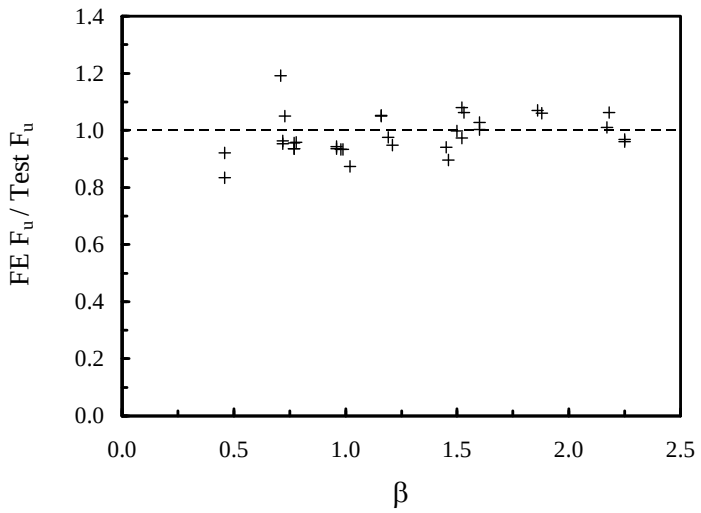

Figure 13: Stub column FE ultimate load divided by test ultimate load versus cross-section slenderness, β

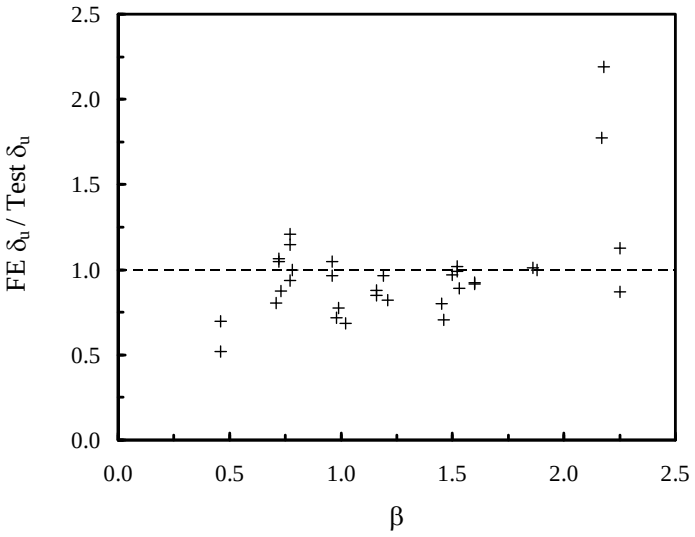

Figure 14: Stub column FE deformation at ultimate load divided by test deformation at ultimate load versus cross-section slenderness, β

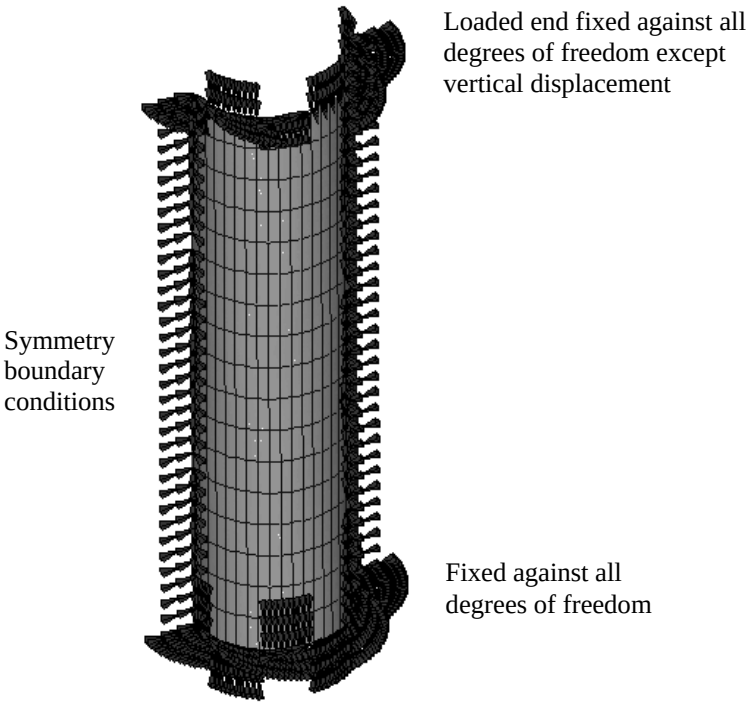

Figure 15: Typical CHS stub column FE model with boundary conditions

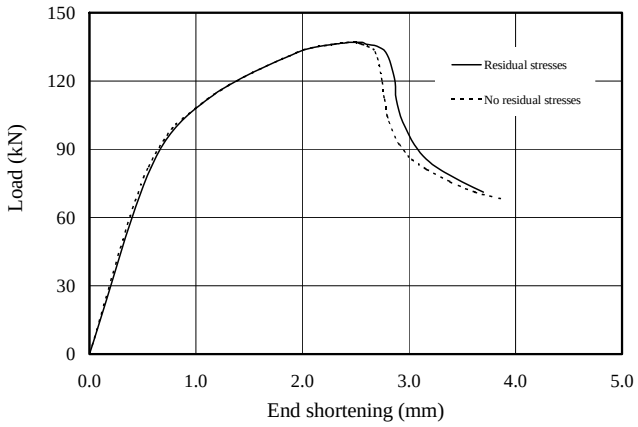

Figure 16: Effect of residual stresses on CHS 100×1.0 stub column FE model

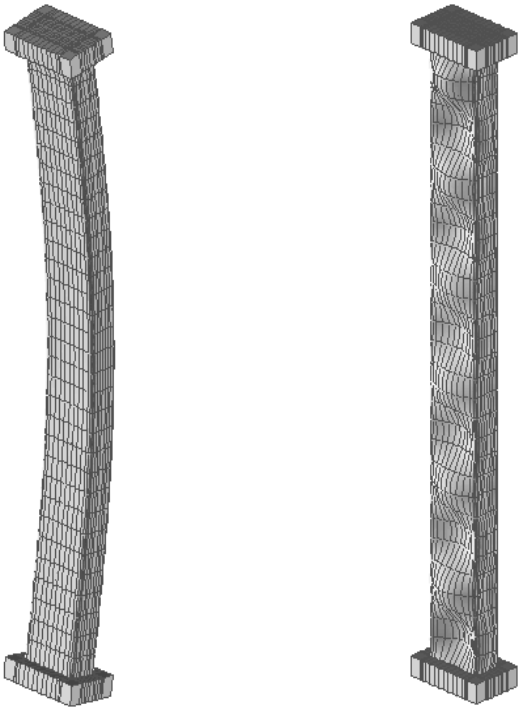

(a) Eigenmode 1:

Global buckling mode

(b) Eigenmode 2:

Local buckling mode

Figure 17: Two lowest eigenmodes for 1m pin-ended RHS 100×50×3

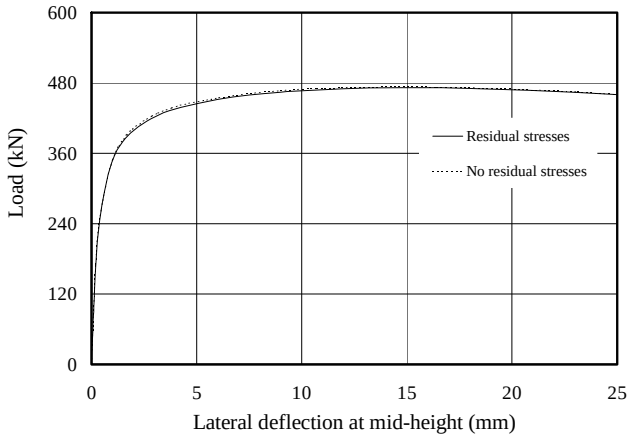

Figure 18: Effect of residual stresses on SHS 100×100×4 pin-ended column FE model

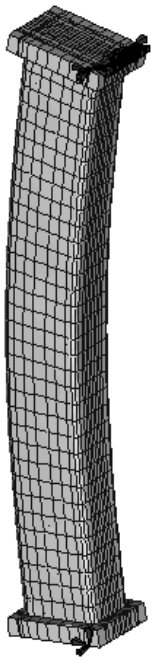

All translational degrees of freedom, except vertical displacement, fixed on a line of nodes adjacent to centreline of wall thickness.

All translational degrees of freedom fixed on a line of nodes adjacent to centreline of wall thickness.

Figure 19: Deformed RHS 150×100×6 (length = 1050 mm) beam-column FE model with boundary conditions

Table 1: Measured and predicted maximum initial imperfection amplitudes for SHS stub columns

Specimen identification (1)	*Measured values (mm)*	*Predicted values (mm)*	*Predicted / Measured (4)*
	u_{max} *(2)*	$\omega_0 / t = 0.023(\sigma_{0.2} / \sigma_{cr})$ *(3)*	
SHS 80×80×4- SC3	0.043	0.022	0.51
SHS 80×80×4- ASC1[1]	0.078	0.013	0.16
SHS 80×80×4- ASC2[1]	0.087	0.013	0.15
SHS 100×100×2- SC1	0.021	0.060	2.88
SHS 100×100×2- SC2	0.030	0.060	2.01
SHS 100×100×3- SC1	0.022	0.041	1.85
SHS 100×100×3- SC2	0.038	0.041	1.08
SHS 100×100×4- SC1	0.038	0.036	0.94
SHS 100×100×4- SC2	0.042	0.036	0.85
SHS 100×100×6- SC1	0.027	0.024	0.88
SHS 100×100×6- SC2	0.032	0.024	0.75
SHS 100×100×8- SC1	0.031	0.011	0.36
SHS 100×100×8- SC2	0.045	0.011	0.25
SHS 150×150×4- SC1	0.072	0.066	0.92
SHS 150×150×4- SC2	0.096	0.067	0.70

Note: [1] Distortions may have been induced due to thermal gradients during the annealing process

Table 2: Measured and predicted maximum initial imperfection amplitudes for RHS stub columns

Specimen identification (1)	*Measured values (mm)*	*Predicted values (mm)*	*Predicted / Measured (4)*
	u_{max} *(2)*	$\omega_0 / t = 0.023(\sigma_{0.2} / \sigma_{cr})$ *(3)*	
RHS 60×40×4- SC1	0.017	0.013	0.78
RHS 60×40×4- SC2	0.022	0.013	0.61
RHS 120×80×3- SC1	0.038	0.061	1.60
RHS 120×80×3- SC2	0.052	0.061	1.18
RHS 120×80×6- SC1	0.016	0.036	2.27
RHS 120×80×6- SC2	0.045	0.036	0.81
RHS 150×100×4- SC1	0.055	0.055	1.00
RHS 150×100×4- SC2	0.039	0.055	1.41
RHS 100×50×2- SC1	0.139	0.063	0.45
RHS 100×50×2- SC2	0.039	0.063	1.92
RHS 100×50×3- SC1	0.055	0.049	0.89
RHS 100×50×3- SC2	0.072	0.049	0.68
RHS 100×50×4- SC1	0.032	0.035	1.11
RHS 100×50×4- SC2	0.048	0.036	0.75
RHS 100×50×6- SC1	0.021	0.027	1.29
RHS 100×50×6- SC2	0.019	0.027	1.42

Table 3: Summary of comparison between FE results and test results for SHS and RHS stub columns

Statistical measure (1)	*Corner properties extended to t*		*Corner properties extended to 2t*	
	FE F_u / Test F_u (2)	*FE δ_u / Test δ_u (3)*	*FE F_u / Test F_u (4)*	*FE δ_u / Test δ_u (5)*
MEAN (using measured imperfections amplitudes):	**0.96**	**0.94**	**0.98**	**0.98**
ST DEV (using measured imperfection amplitudes):	0.07	0.20	0.07	0.30
MEAN (using predicted imperfections amplitudes):	**0.97**	**1.00**	**1.00**	**1.06**
ST DEV (using predicted imperfection amplitudes):	0.09	0.21	0.09	0.30

Table 4: Comparison between CHS stub column tests and FE models with different levels of local geometric imperfection amplitude, ω_0

CHS specimen identification (1)	*ω_0 = 0.01t (2)*		*ω_0 = 0.1t (3)*		*ω_0 = 0.2t (4)*		*ω_0 = 0.5t (5)*	
	Test F_u / FE F_u	*Test δ_u / FE δ_u*	*Test F_u / FE F_u*	*Test δ_u / FE δ_u*	*Test F_u / FE F_u*	*Test δ_u / FE δ_u*	*Test F_u / FE F_u*	*Test δ_u / FE δ_u*
103×1.5- SC1	1.09	0.91	1.09	0.94	1.10	0.96	1.04	0.71
103×1.5- SC2	1.06	0.88	1.05	0.91	1.04	0.90	1.01	0.69
101.6×2.85- SC1	1.09	1.29	1.09	1.30	1.10	1.21	1.00	0.96
101.6×2.85- SC2	1.09	1.10	1.09	1.10	1.10	1.15	0.99	0.81
101.6×2.85- SC3	1.08	0.89	1.08	0.91	1.08	0.93	1.01	0.71
140×2- SC	1.05	0.83	1.05	0.83	1.05	0.90	0.96	0.54
140×3- SC	0.87	0.54	0.87	0.55	0.87	0.60	0.83	0.41
140×4- SC	0.98	0.98	0.98	0.99	0.98	1.18	0.93	0.65
153×1.5- SC1	0.98	0.91	0.98	0.92	0.98	1.07	0.93	0.60
153×1.5- SC2	0.99	1.18	0.99	1.18	0.99	1.21	0.96	0.85
MEAN:	**1.03**	**0.95**	**1.03**	**0.96**	**1.03**	**1.01**	**0.97**	**0.69**
ST DEV:	**0.07**	**0.21**	**0.07**	**0.21**	**0.07**	**0.19**	**0.06**	**0.16**

Table 5: Comparison between all SHS pin-ended column test results and FE results

Specimen identification (1)	*β (2)*	*$\bar{\lambda}$ (3)*	*Test F_u (kN) (4)*	*FE F_u (kN) (5)*	*Test F_u/FE F_u (6)*
SHS 40×40×4- LC1	0.51	1.07	184	171	0.93
SHS 40×40×4- LC2	0.51	1.07	184	168	0.91
SHS 60×60×5- LC1	0.57	0.75	417	397	0.95
SHS 60×60×5- LC2	0.57	1.22	235	229	0.97
SHS 60×60×5- LC3	0.57	1.68	137	138	1.01
SHS 80×80×3-LC1	1.18	0.47	390	401	1.03
SHS 80×80×3-LC2	1.18	0.94	193	242	1.25
SHS 80×80×3-LC3	1.18	1.42	96	143	1.49
SHS 80×80×4-LC1	0.91	0.89	307	313	1.02
SHS 80×80×4-LC2	0.92	0.94	293	294	1.00
SHS 100×100×2-LC1	2.23	0.67	176	167	0.95
SHS 100×100×3-LC1	1.46	0.68	350	328	0.94
SHS 100×100×4-LC1	1.18	0.76	464	472	1.02
SHS 100×100×6-LC1	0.78	0.82	842	755	0.90
SHS 100×100×8-LC1	0.46	0.69	770	871	1.13
SHS 150×150×4- LC1	1.51	0.42	692	-[1]	-
MEAN:					**1.03**
ST DEV:					**0.16**

Note: [1] Convergence problems prevented solution

Table 6: Comparison between all RHS minor axis buckling pin-ended column test results and FE results

Specimen identification (1)	*β (2)*	*$\bar{\lambda}$ (3)*	*Test F_u (kN) (4)*	*FE F_u (kN) (5)*	*Test F_u/FE F_u (6)*
RHS 60×40×4-LC1	0.72	1.02	169	188	1.11
RHS 100×50×2-LC1	2.28	0.64	163	132	0.81
RHS 100×50×3-LC1	1.62	0.73	304	286	0.94
RHS 100×50×4-LC1	1.19	0.72	422	364	0.86
RHS 100×50×6-LC1	0.77	0.80	624	603	0.97
RHS 120×80×3-LC1	1.91	0.45	448	427	0.95
RHS 100×50×3-LC1	1.61	1.46	113	135	1.19
RHS 100×50×4-LC1	1.20	1.45	165	160	0.97
RHS 100×50×6-LC1	0.77	1.61	234	219	0.94
RHS 120×80×3-LC1	1.88	0.90	313	310	0.99
RHS 120×80×6-LC1	0.96	0.99	677	612	0.90
RHS 150×100×4-LC1	1.54	0.62	515	501	0.97
MEAN:					**0.97**
ST DEV:					**0.10**

Table 7: Comparison between all RHS major axis buckling pin-ended column test results and FE results

Specimen identification (1)	*β (2)*	$\bar{\lambda}$ *(3)*	*Test* F_u *(kN) (4)*	*FE* F_u *(kN) (5)*	*Test* F_u*/FE* F_u *(6)*
RHS 60×40×4-LC1	0.72	1.47	109	118	1.08
RHS 100×50×2-LC1	2.27	0.75	157	141	0.90
RHS 150×100×3- LC1	1.96	0.58	349	357	1.02
RHS 150×100×3- LC2	1.96	0.94	254	253	1.00
RHS 150×100×3- LC3	1.96	1.29	189	176	0.93
RHS 150×100×6- LC1	0.93	0.59	830	860	1.04
RHS 150×100×6- LC2	0.95	0.95	488	535	1.10
RHS 150×100×6- LC3	0.95	1.31	306	340	1.11
MEAN:					**1.02**
ST DEV:					**0.08**

Table 8: Comparison between all SHS and RHS beam-column test results and FE results

Specimen identification (1)	*β (2)*	*$\bar{\lambda}$ (3)*	*Test F_u (kN) (4)*	*FE F_u (kN) (5)*	*Test F_u/FE F_u (6)*
SHS 60×60×5- BC1	0.72	1.47	322	290	0.90
SHS 60×60×5- BC2	2.27	0.75	210	196	0.93
SHS 60×60×5- BC3	1.96	0.58	125	122	0.98
SHS 60×60×5- BC4	1.96	0.94	83	82	0.99
RHS 150×100×3- BC1	1.96	1.29	209	202	0.97
RHS 150×100×3- BC2	0.93	0.59	173	171	0.99
RHS 150×100×3- BC3	0.95	0.95	134	126	0.94
RHS 150×100×3- BC4	1.96	0.58	95	93	0.98
RHS 150×100×6- BC1	1.96	0.94	569	577	1.01
RHS 150×100×6- BC2	1.96	1.29	403	400	0.99
RHS 150×100×6- BC3	0.93	0.59	267	272	1.02
RHS 150×100×6- BC4	0.95	1.31	192	194	1.01
MEAN:					**0.98**
ST DEV:					**0.04**

Note: All beam-column tests conducted by Talja and Salmi (1995)

Figure captions

Figure 1: Idealized weld-induced residual stress distribution for SHS and RHS

Figure 2: Residual stress measurements in welded carbon steel CHS (Chen and Ross, 1977)

Figure 3: Projected CHS residual stress model proposed by Gao et al. (1998)

Figure 4: Four lowest eigenmodes for an SHS 80×80×3 stub column

Figure 5: Comparison of imperfection amplitudes from independent specimens

Figure 6: Measured versus predicted imperfection amplitudes for $\omega_0 / t = 0.023(\sigma_{0.2}/\sigma_{cr})$

Figure 7: Imperfection sensitivity of 2m SHS 80×80×4 pin-ended column for global imperfection amplitudes ranging from L /100 to L /10000

Figure 8: Boundary conditions applied to SHS and RHS stub column FE models

Figure 9: Extents of corner regions in FE models

Figure 10: Effect of residual stresses on 100×100×2 stub column FE model

Figure 11: Effect of residual stresses on 80×80×4 stub column FE model

Figure 12: Failure mode from SHS 100×100×2- SC1 stub column test and corresponding FE model

Figure 13: Stub column FE ultimate load divided by test ultimate load versus cross-section slenderness, β

Figure 14: Stub column FE deformation at ultimate load divided by test deformation at ultimate load versus cross-section slenderness, β

Figure 15: Typical CHS stub column FE model with boundary conditions

Figure 16: Effect of residual stresses on CHS 100×1.0 stub column FE model

Figure 17: Two lowest eigenmodes for 1m pin-ended RHS 100×50×3

Figure 18: Effect of residual stresses on SHS 100×100×4 pin-ended column FE model

Figure 19: Deformed RHS 150×100×6 (length = 1050 mm) beam-column FE model with boundary conditions